 doi:10.20944/preprints202210.0449.v1

Article

Surface water extent mapping in Denmark: Comparing airborne thermal imagery and satellite earth observation

Peter Bauer-Gottwein [1,*], Henrik Grosen [2], Daniel Druce [3], Christian Tøttrup [4], Heidi E. Johansen [5], Roland Löwe [6]

[1] Department of Environmental and Resource Engineering, Technical University of Denmark; 2800 Kgs. Lyngby, Denmark, pbau@dtu.dk
[2] Drone Systems, 8200 Aarhus, Denmark, henrik@dronesystems.dk
[3] DHI, 2970 Hørsholm, Denmark, dadr@dhigroup.com
[4] DHI, 2970 Hørsholm, Denmark, cto@dhigroup.com
[5] Jammerbugt Kommune, 9440 Aabybro, Denmark, hbj@jammerbugt.dk
[6] Department of Environmental and Resource Engineering, Technical University of Denmark; 2800 Kgs. Lyngby, Denmark, rolo@dtu.dk
* Correspondence: pbau@dtu.dk

Abstract: Mapping and prediction of inundated areas is increasingly important for climate change adaptation and emergency preparedness. Flood forecasting tools and flood risk models have to be compared to observed flooding patterns for training, calibration, validation and benchmarking. At regional to continental scale, satellite earth observation is the established method for surface water extent (SWE) mapping and several operational global-scale data products are available. However, the spatial resolution of satellite-derived SWE maps remains a limiting factor, especially in low-lying areas with complex hydrography, such as Denmark. We collected thermal imagery using an unmanned airborne system (UAS) for three areas in Denmark shortly after major flooding events. We combined the thermal imagery with an airborne lidar-derived high-resolution digital surface model of the country to retrieve high-resolution (40 cm) SWE maps. The resulting SWE maps were compared to low-resolution SWE maps derived from satellite earth observation (EO). We conclude that UAS have significant potential for SWE mapping at intermediate scales, can bridge the scale gap between ground observations and satellite EO and can be used to benchmark and validate SWE mapping products derived from satellite EO as well as models predicting inundation.

Keywords: surface water extent; satellite earth observation; unmanned airborne systems

1. Introduction

Frequency and severity of extreme flooding events are expected to increase around the world because of human-induced climate change. Flood risk assessment and flood forecasting are essential tools for climate change adaptation. Such tools operate over a range of scales, spanning from local or city scale [1] to regional-continental [2] or even global scale [3,4]. Input data and model parameterization have significant impacts on the simulated flooding patterns produced by such tools [5]. The most sensitive input dataset is the digital elevation model of the terrain and a highly sensitive model parameters are the hydraulic roughnesses of river channels and surrounding floodplains [6]. The best currently available global DEMs have a spatial resolution of around 30m and a vertical accuracy of a couple of meters [7,8], which is insufficient for accurate simulation of overland flow in complex landscapes and floodplains. Hydraulic roughness is generally not directly observable and is typically determined using hydraulic inverse modeling workflows [9].

It is thus essential to train, calibrate and/or validate flood risk assessment tools and flood forecasting models against observed flooding patterns / surface water extent maps. Over the past decade, a number of global-scale surface water extent datasets derived from

 doi:10.20944/preprints202210.0449.v1

satellite EO datasets have become available [10–12]. While such datasets have been impactful and effective in order to understand and quantify surface water status at continental to global scale, their coarse spatial resolution limits applications at local-regional scale, especially in low lying areas with complex hydrography that are characterized by small ephemeral water bodies forming in response to extreme rainfall events.

Remote sensing methods using unmanned airborne systems (UAS) are a promising monitoring option at local-regional scales, because they can deliver sub-meter spatial resolution and can be scheduled flexibly in space and time at relatively low cost [13]. UAS thermal imaging is a mature technique that has been used for many applications, including utility mapping [14], vegetation/agriculture status assessment [15,16] and river flow tracking [17].

This paper presents a SWE mapping method based on UAS thermal imagery. The workflow is demonstrated for three areas in Denmark, in which flooding occurs at small spatial scales. UAS SWE maps are compared with SWE maps derived from satellite EO. Advantages and disadvantages of the two alternative mapping methods are discussed in view of typical application scenarios and end user requirements.

2. Materials and Methods

We first provide an overview of the survey sites and flooding events selected for this study. Subsequently, we describe the SWE mapping workflow based on UAS thermal imagery, which was applied at the sites. Finally, we present the SWE mapping workflow based on satellite EO datasets.

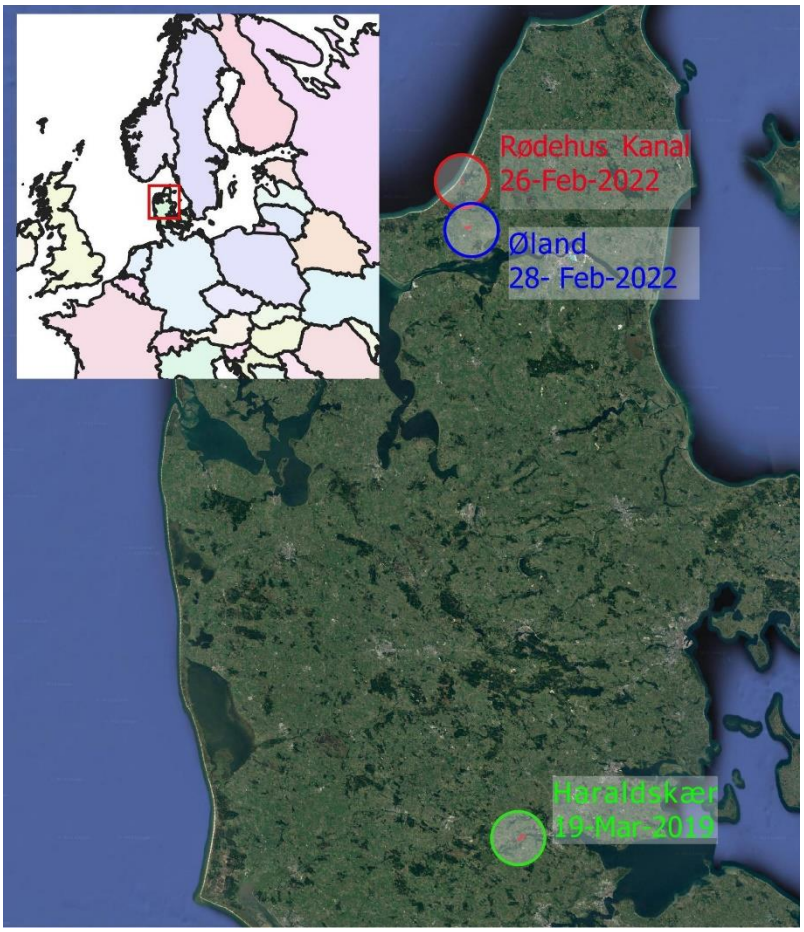

Figure 1. Overview of thermal survey sites and dates. Inset map shows the location of the study sites in Europe.

Preprints (www.preprints.org) | NOT PEER-REVIEWED | Posted: 28 October 2022 doi:10.20944/preprints202210.0449.v1

2.1. Sites and flooding events

Figure 1 provides and overview of localities mapped with UAS thermal imagery and satellite EO. The Rødehus Kanal and Øland areas are located in the Danish Jammerbugt municipality. The UAS surveys were flown on February 26th and February 28th, 2022, respectively. February 2022 was a wet month in Jammerbugt municipality (Figure 2). The monthly rainfall was 105.8 mm (long-term average for February in Denmark: 48 mm). The cumulative precipitation in the 7 days prior to the UAS thermal surveys was 33.2 mm and the cumulative precipitation in the 14 days prior to the survey was 73.5 mm.

The Haraldskær area is located in the Danish Vejle municipality. The UAS survey was flown on March 19th, 2019. March 2019 was a wet month in Vejle municipality (Figure 2). The monthly rainfall was 139.9 mm (long-term average for March in Denmark: 52 mm). The cumulative precipitation in the 7 days prior to the thermal survey was 66.9 mm and the cumulative precipitation in the 14 days prior to the survey was 112.8 mm. Flooding was informally observed on the ground in late February 2022 in Jammerbugt municipality, and in March 2019 in Vejle municipality by citizens and local media.

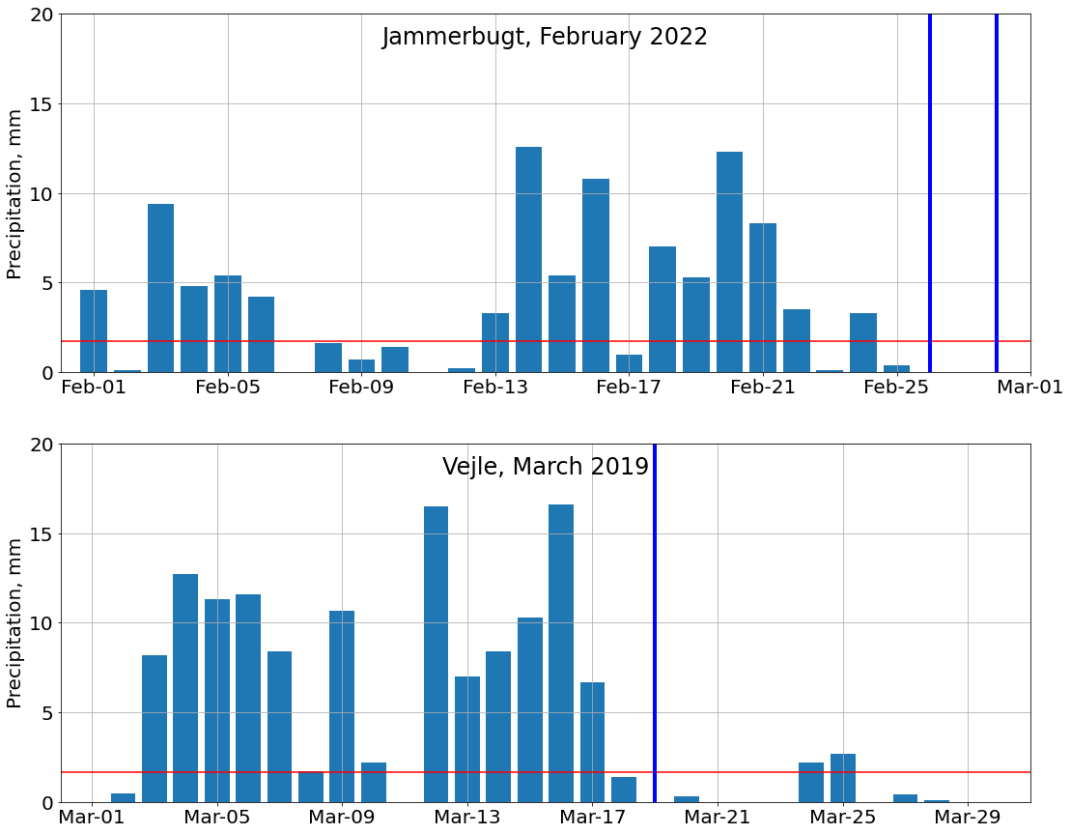

Figure 2. Daily rainfall time series for Jammerbugt and Vejle municipalities in February 2022 and March 2019, respectively. Red lines indicate long-term average precipitation. Data provided by the Danish Meteorological Institute through their "Vejrarkiv" web interface (www.dmi.dk/vejrarkiv/). Vertical blue lines indicate dates of UAS thermal surveys.

2.2. Surface water extent mapping with UAS thermal imagery

RGB and thermal mapping using UAS have become mature surveying techniques providing ground resolution at the cm level and flexible spatial and temporal coverage. Flooding can be delineated from both RGB and thermal imagery. Here, we opted for a thermal mapping workflow, because thermal mapping is independent of daylight conditions, which pose severe restrictions on survey schedules in Denmark in winter, and because thermal mapping can reliably detect shallow flooding below low-density vegetation for instance in grasslands and agricultural areas.

 doi:10.20944/preprints202210.0449.v1

Drone Systems collected thermal imagery using a FLIR Tau-2 thermal camera (Teledyne FLIR, Wilsonville, Oregon, USA) equipped with a TeAX thermal capture system (TeAX, Wilnsdorf, Germany). Surveys were flown using a Matrice 600 Pro (DJI, Shenzhen, China) platform. Survey flight height was 110-120m above ground, which resulted in a 15 cm ground resolution of the thermal imagery. Thermal imagery was corrected for drift and sensor non-uniformity artifacts, mosaicked and subsequently georeferenced using terrain features that could be detected on both the thermal scene and high-resolution airborne imagery. The thermal mapping workflow used here is equivalent to Drone Systems commercial surveying service [18]. An example of the output of the thermal mapping workflow is provided in Figure 3 for the Rødehus Kanal area.

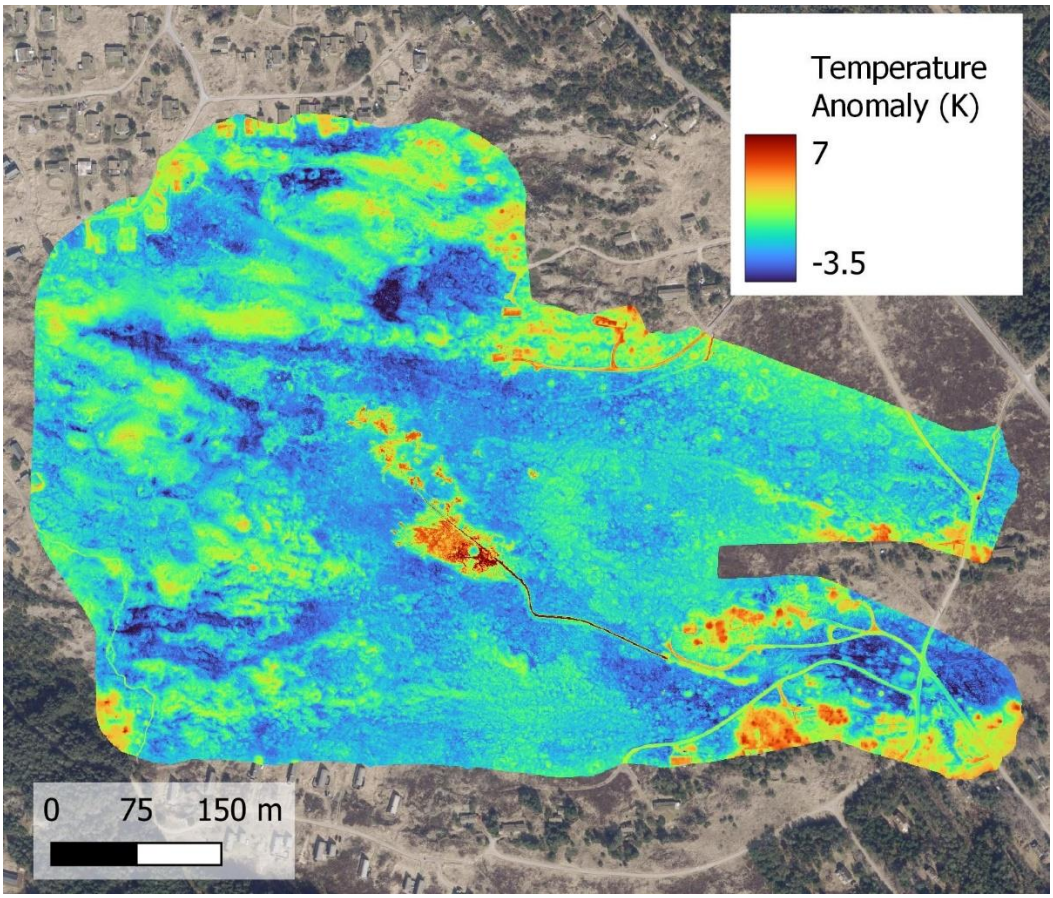

Figure 3. Thermal anomaly map (in Kelvin) for the Rødehus Kanal area. Temperature anomaly is defined as temperature at each pixel minus average temperature of the scene.

From Figure 3, it is evident that open water and flooded areas are warmer than the surroundings in this situation. This is common for flooding events occurring during the cold season. However, it is also evident that warm temperature anomalies occur not only on flooded areas, but also on vegetated areas and buildings, i.e. whenever the thermal camera does not record the ground surface temperature, but the temperature of an intermediate surface, such as the top of the canopy or the rooftop of a house. Buildings are typically warmer than the surroundings in the cold season because they are heated. We also observe warmer temperature on canopy surfaces, possibly because rainwater storage on the canopy, or because of the higher elevation of canopy surfaces and strong temperature gradients in the atmospheric surface layer.

In order to mask buildings and areas covered by vegetation canopy we use the Danish national elevation model (Danmarks Højdemodel, [19]), which is derived from airborne laser scanning surveys covering the entire country. The raw laser point cloud, consisting of 415 billion individual points, was processed into a digital surface model at 0.4m

Preprints (www.preprints.org) | NOT PEER-REVIEWED | Posted: 28 October 2022 doi:10.20944/preprints202210.0449.v1

spatial resolution [20], which is publicly available on the internet. The digital surface model (DSM) was further processed into a digital terrain model (DTM, [21], also at 0.4m spatial resolution), by removing buildings, vegetation etc. from the digital surface model and interpolating the underlying terrain elevation from neighboring points. We calculate the elevation difference between the DSM and the DTM. Whenever this difference exceeds 1m, we assume that the thermal camera does not map ground temperature and, consequently, we mask the corresponding area and exclude it from the surface water extent map, setting the pixel value to undefined (NaN). The flooding status of the masked areas cannot be determined from airborne thermal imagery. We calculated the local sensitivity of the masked area to the 1m elevation difference threshold and found a limited sensitivity of 26.2 m^2 of masked area per square kilometer of terrain per m of threshold change for the Rødehus Kanal area (16.3 $m^2/km^2/m$ for Vejle and 2.5 $m^2/km^2/m$ for Øland). For this reason, the 1m threshold in elevation difference can be considered as robust and we applied it consistently throughout the analysis.

Finally, we manually threshold the masked temperature image in order to obtain a binary SWE map. Pixels that are warmer than the threshold are assigned flooded status (1), and pixels that are cooler than the threshold are assigned dry status (0). Masked areas and areas not covered by the thermal imagery are assigned undetermined flooding status (NaN). The temperature threshold is set based on the observed temperature of permanent water bodies (streams, lakes) located in the thermal image. A flowchart of the UAS SWE mapping workflow is presented in Figure 4.

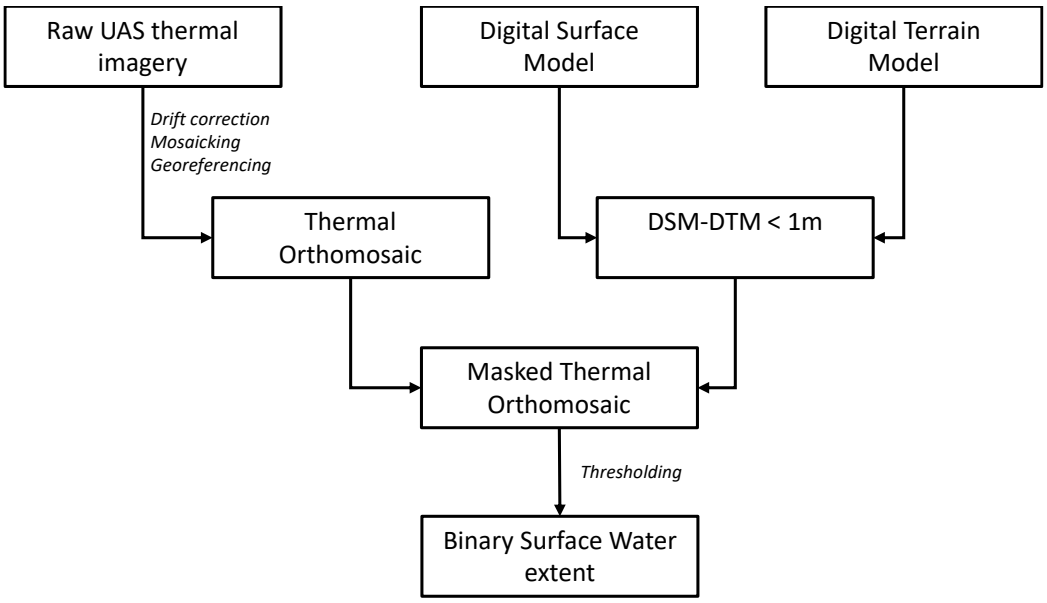

Figure 4. Flow chart of the surface water extent mapping workflow based on UAS thermal imagery

2.3. Surface water extent mapping with satellite EO

The approach for SWE mapping using satellite EO data is documented in [22]. The approach uses a multivariate logistic regression model to estimate surface water probability from a combination of optical imagery from the Sentinel-2 mission and synthetic aperture radar (SAR) imagery from the Sentinel-1 mission. In the original approach by Druce et al. [22], the input data are processed into monthly composites, but, specifically for Danish conditions, we modified the algorithm to output the results by individual sensor and acquisition date, thereby enabling the surface water extent products to correspond with the time of the flooding / drone activity. Optical data was prioritized where available due to the ability to identify smaller features than Sentinel-1. This is explained by the characteristics of the input data, with key spectral water detection bands from Sentinel-2

 doi:10.20944/preprints202210.0449.v1

available in 10-m spatial resolution, while the true spatial resolution of Sentinel-1 is understood to be closer to 20 × 20 m, although data from the widely used Sentinel-1 Ground Range Detection (GRD) product are delivered with a pixel spacing of 10x10m [23]. In addition, SAR imagery is typically spatially smoothed to reduce speckle noise. Nevertheless, optical data will often be redundant at the time of flooding due to the presence of clouds. After sensor selection, the resulting water probability was inspected, and a user defined threshold applied to create the binary surface water extent classification.

2.4. Validation against the hydrographically processed DEM

The Danish national elevation model was further processed by the Danish Agency for Data Supply and Infrastructure into a so-called Bluespot product [24]. The pixel value of the Bluespot product indicates the amount of rainfall in millimeters that is required to flood the pixel. This value is derived under the assumptions that the terrain surface is impervious (i.e. zero infiltration, no drainage), that the rainfall is uniformly distributed in space, that evapotranspiration is zero and that water on the land surface moves instantaneously against the terrain elevation gradient and accumulates in local depressions. The Bluespot product thus indicates areas of potential flooding caused by rainfall, and it is therefore useful to compare the product with the SWE maps derived from UAS and satellite EO. However, it is important to note that the Bluespot product outlines areas of potential flooding, and that actual flooding is expected to occur only on a subset of Bluespot areas, because some Bluespot areas may be located on soils with high infiltration capacity and/or drained areas. Moreover, riverine flooding (i.e. flooding caused by river water flowing over the riverbanks) will not be confined to Bluespot areas, because it is not caused by local rainfall and will not only occur in local depressions.

3. Results

In this section, we present the SWE mapping results for the three survey sites separately.

Figure 5 shows UAS and satellite EO SWE mapping results along with Bluespot areas for the Rødehus Kanal site. It is evident that the UAS workflow delineates flooding mainly along a small stream flowing across the site (Figiure 5, panel B). About half of the inundated area delineated from thermal imagery does not fall on Bluespot areas (Table 1). This is consistent with the riverine origin of the flooding. The satellite SWE mapping workflow classifies just 4 10m pixels falling within the boundaries of the thermal scene as flooded, based on a Sentinel-1 SAR scene recorded on 28-02-2022 (Figure 5, panels A and C). In order to compare Bluespot and UAS flood maps with 0.4m spatial resolution to the satellite SWE mapping results with 10m resolution, we aggregate the binary Bluespot and UAS flooding maps to 10m resolution using an “any pixel” rule. This rule implies that the 10m pixel is assigned a value of 1, if any of the 0.4m pixels falling on each 10m pixel have a value of 1; otherwise, the pixel is assigned a value of 0. Table 1 reports contingency tables between the Bluespot product and the satellite SWE maps as well as between the UAS and satellite SWE maps. All pixels classified as flooded based on satellite EO fall on Bluespot areas. However, despite the use of the “any pixel” aggregation rule, which enlarges the area classified as flooded compared to the native 0.4m resolution, none of the 4 pixels classified as flooded based on satellite EO fall on pixels that are delineated as flooded by the UAS workflow. The flooded areas delineated using the UAS workflow are hydrologically consistent, occurring mainly adjacent to the stream, which was likely flooding after the substantial rainfall in February 2022. In contrast, the flooded areas delineated by satellite EO appear to be randomly located in the landscape and were not confirmed by informal observations on the ground.

Preprints (www.preprints.org) | NOT PEER-REVIEWED | Posted: 28 October 2022 doi:10.20944/preprints202210.0449.v1

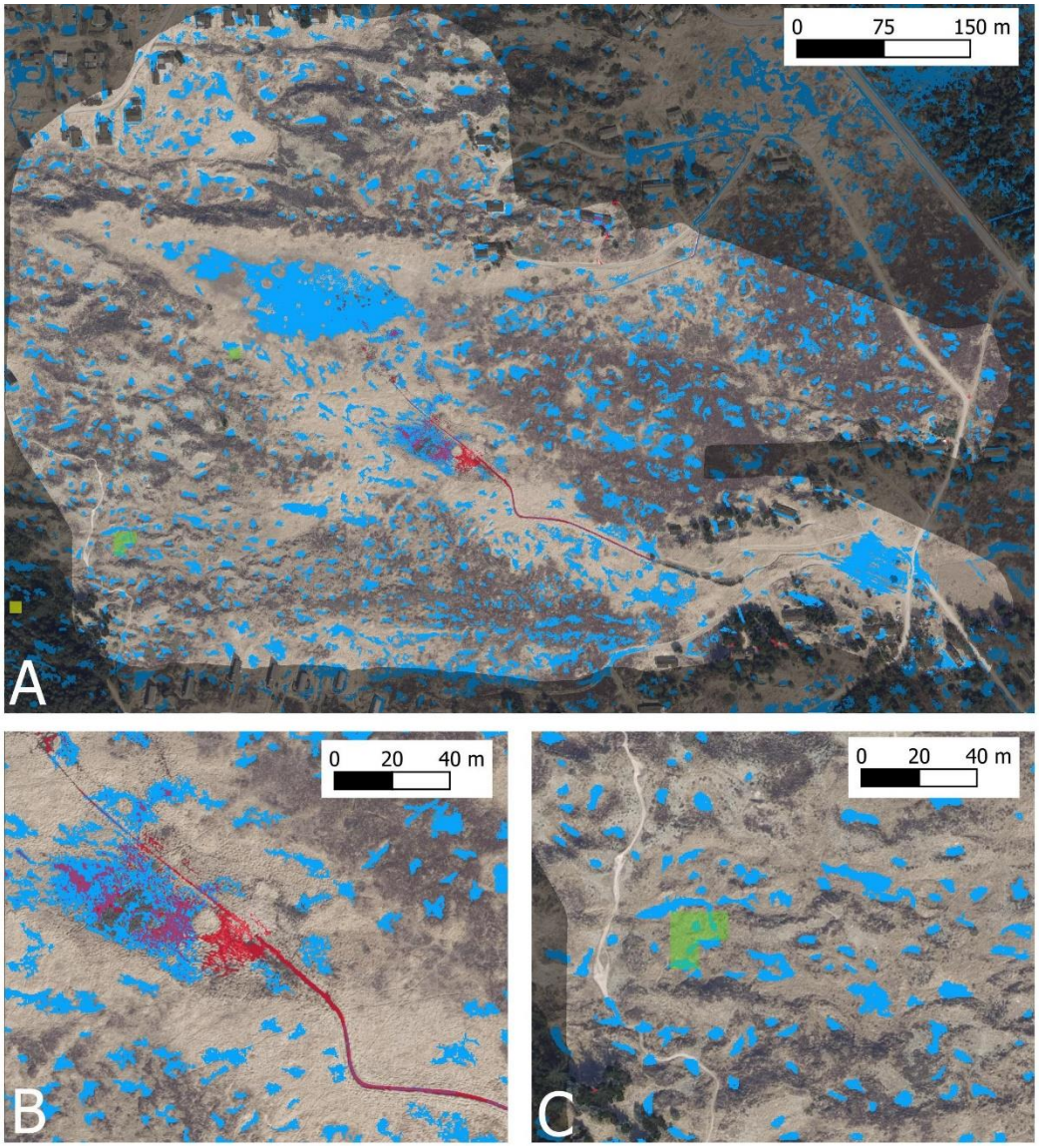

Figure 5. Blue Spot areas (blue, threshold 10mm), UAS SWE (red) and Satellite SWE (green: Sentinel-1, 28-02-2022, yellow: Sentinel-2, 26-02-2022) for the entire Rødehus Kanal area (A) and two zoomed-in sub-areas (B,C). Background is spring airborne imagery and grey shading indicates areas without UAS flooding status.

 doi:10.20944/preprints202210.0449.v1

Table 1. Contingency table for the Rødehus Kanal area. We only report contingency tables for Sentinel-1 SWE, because the only pixel mapped as flooded by Sentinel-2 is located outside the thermal scene.

Blue Spot vs UAS SWE (0.4 m pixels)		
	Inside Blue Spot	Outside Blue Spot
UAS flooded	6435	6468
UAS not flooded	281799	1917380
Blue Spot vs Satellite SWE (10 m pixels)		
	Inside Blue Spot	Outside Blue Spot
Sentinel-1 flooded	4	0
Sentinel-1 not flooded	2610	1199
UAS vs Satellite SWE (10 m pixels)		
	Sentinel-1 flooded	Sentinel-1 not flooded
UAS flooded	0	189
UAS not flooded	4	3620

Figure 6 shows UAS and satellite EO SWE mapping results along with Bluespot areas for the Øland site. Unlike the Rødehus Kanal site, the Øland site includes two permanent lakes, which are reliably classified as flooded by both the UAS and the satellite flood mapping workflows (Figure 6, panel B). It is evident from the results that the Sentinel-1 SAR-based mapping delineates a smaller area of the permanent lakes than the mapping based on Sentinel-2 multispectral data, and that the Sentinel-2 multispectral results are in better agreement with the UAS results than the Sentinel-1 SAR results. On Figure 6, panel B, Sentinel-2 misclassifies some pixels located in the shaded area of the forest as water. We see similar behavior in the Haraldskær area (see below). While the satellite EO mapping workflow reliably maps the permanent lakes, it does not detect any flooded areas on open fields. In contrast, the UAS mapping workflow identifies at least five hotspot areas of flooding in the open agricultural fields. The majority of the areas mapped as flooded by the UAS workflow fall on Bluespot areas, which supports the validity of the UAS mapping workflow, because these floods clearly are of pluvial origin. One sizeable patch of flooded terrain in the UAS results does not fall on a Bluespot area (white circle in Figure 6, panel C). This patch falls on a field on which the ploughing direction has changed between the date when the national elevation dataset was acquired and the date of thermal mapping. It is evident from the Bluespot dataset in this area that the field was ploughed in north-south direction at the time of laser scanning for the national elevation dataset, while the UAS thermal mapping indicates ploughing in east-west direction. This shows that in flat terrain, minor changes in elevation can determine the location of pluvial inundation patches. Table 2 provides contingency tables for the comparisons between UAS, satellite and Bluespot datasets. Bluespot and UAS results were upscaled to 10m using an “any pixel” rule as described for the Rødehus Kanal area.

Preprints (www.preprints.org) | NOT PEER-REVIEWED | Posted: 28 October 2022 doi:10.20944/preprints202210.0449.v1

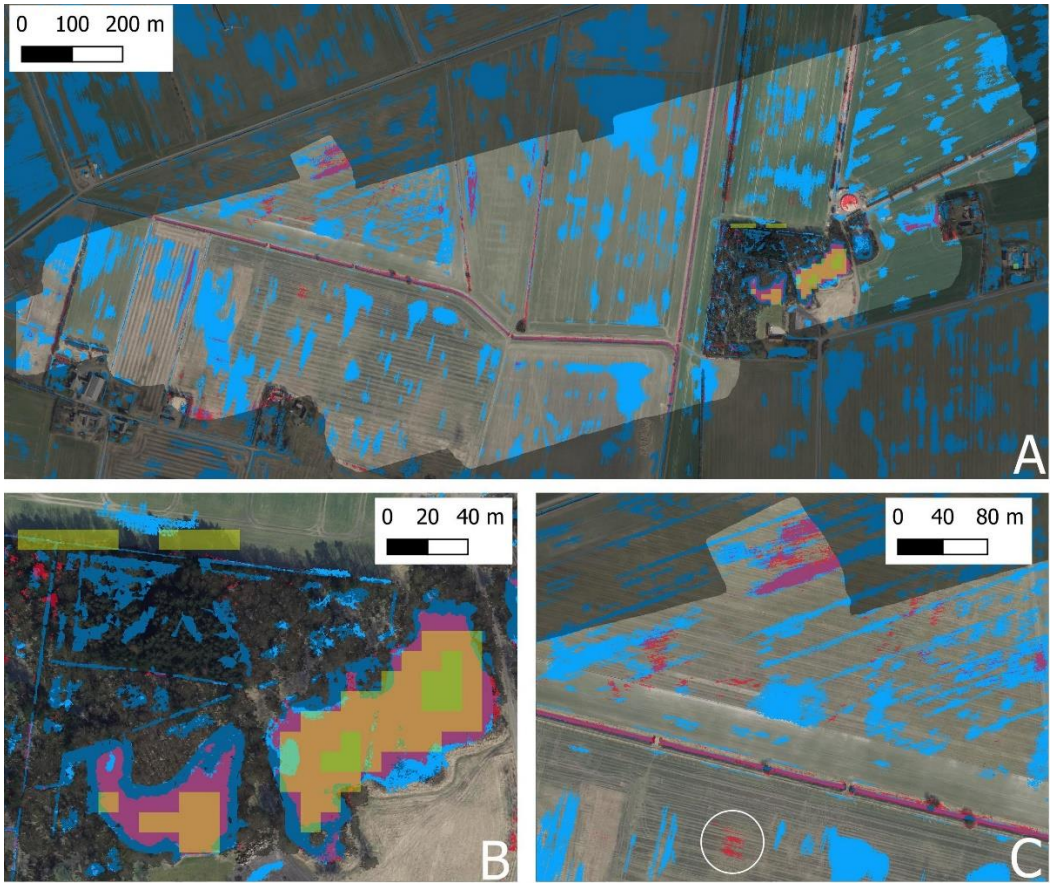

Figure 6. Blue Spot areas (blue, threshold 10mm), UAS SWE (red) and Satellite SWE (green: Sentinel-1, 28-02-2022, yellow: Sentinel-2, 26-02-2022) for the Øland area and two zoomed-in sub-areas. Background is spring airborne imagery and grey shading indicates areas without UAS flooding status. White circle highlights patch of UAS-flooded pixels outside Blue Spot area.

Table 2. Contingency table for the Øland area

Blue Spot vs UAS SWE (0.4 m pixels)		
	Inside Blue Spot	Outside Blue Spot
UAS flooded	115146	61418
UAS not flooded	969260	4656767
Blue Spot vs Satellite SWE (10 m pixels)		
	Inside Blue Spot	Outside Blue Spot
Sentinel-1 flooded	8	0
Sentinel-1 not flooded	5306	4729
Blue Spot vs Satellite SWE (10 m pixels)		
	Inside Blue Spot	Outside Blue Spot
Sentinel-2 flooded	63	3
Sentinel-2 not flooded	5251	4726
UAS vs Satellite SWE (10 m pixels)		
	Sentinel-1 flooded	Sentinel-1 not flooded
UAS flooded	8	2406
UAS not flooded	0	7629
UAS vs Satellite SWE (10 m pixels)		
	Sentinel-2 flooded	Sentinel-2 not flooded
UAS flooded	59	2355
UAS not flooded	7	7622

Preprints (www.preprints.org) | NOT PEER-REVIEWED | Posted: 28 October 2022 doi:10.20944/preprints202210.0449.v1

Figure 7 shows UAS and satellite EO SWE mapping results along with Bluespot areas for the Haraldskær site. Haraldskær is the largest of the three sites and both the satellite EO and the UAS mapping workflows delineate sizeable areas of both pluvial and riverine flooding (Table 3). In general, there is good agreement between the flooded areas outlined by the satellite EO and the UAS workflow. Flooded areas caused by riverine flooding outlined by the UAS workflow tend to be slightly larger (Figure 7, panel B) as the ones outlined by satellite EO. Similar behavior was observed on the permanent lakes in the Øland area. Just as in the Øland area, Sentinel-2 risks misclassifying pixels as flooded that are located in forested or shaded areas (Figure 7, panels C and D). It is evident from Figure 7, panel E, that flooded areas tend to locate on Bluespot areas. However, only a fraction of Bluespot areas get flooded, while others remain dry.

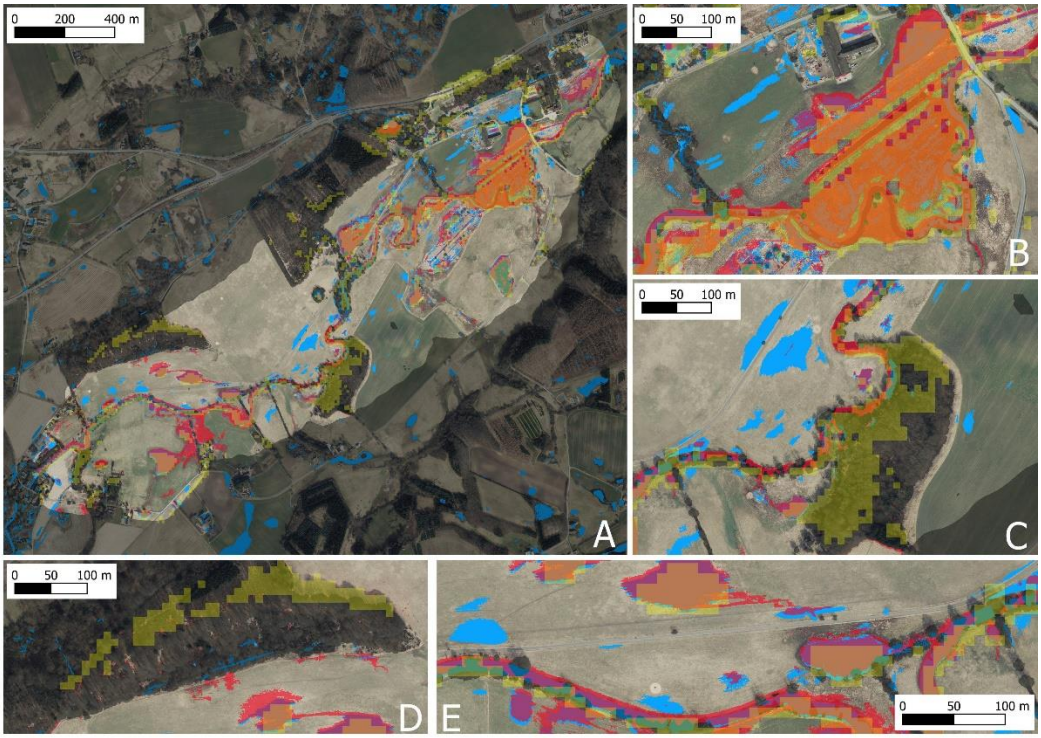

Figure 7. Blue Spot areas (blue, threshold 10mm), UAS SWE (red) and Satellite SWE (yellow: Sentinel-2) for the Haraldskær area and four zoomed-in sub-areas. Background is spring airborne imagery and dark grey shading indicates areas without UAS flooding status. Panel A is the overview of the Haraldskær area and B-E are zoomed-in sub-areas.

Table 3 reports the contingency tables for the comparisons between UAS, satellite EO and Bluespot areas. The majority of areas classified as flooded by both the UAS and satellite EO workflow are located inside Bluespot areas. However, a sizeable fraction of the flooded pixels falls outside the Bluespot areas, which is consistent with the riverine flooding occurring in the downstream portion of the Haraldskær area (Figure 7, panel B). Table 3 shows that the flooded area mapped by UAS is significantly larger than the area mapped as flooded from Sentinel-2. One reason is the "any pixel" rule used to resample the UAS flooding maps from 40cm resolution to 10m resolution. Another reason is the Sentinel-2 under-estimation of the flooded areas along the fringes of water bodies, which was observed both in the Øland and Haraldskær areas.

 doi:10.20944/preprints202210.0449.v1

Table 3. Contingency table for the Haraldskær area. We only report contingency tables for Sentinel-2 SWE, because no Sentinel-1 results are available for the date of the UAS thermal survey.

Blue Spot vs UAS SWE (0.4 m pixels)		
	Inside Blue Spot	Outside Blue Spot
UAS flooded	547657	672873
UAS not flooded	351367	7908880
Blue Spot vs Satellite SWE (10 m pixels)		
	Inside Blue Spot	Outside Blue Spot
Sentinel-2 flooded	1426	1168
Sentinel-2 not flooded	2471	13049
UAS vs Satellite SWE (10 m pixels)		
	Sentinel-2 flooded	Sentinel-2 not flooded
UAS flooded	1984	3470
UAS not flooded	610	12050

4. Discussion

Predicting flood risk and forecasting actual flooding becomes ever more important with increasing frequency, severity and impact of flood events. At the same time, mapping surface water extent remains challenging, particularly for low-gradient environments with complex hydrography and small-scale flooding patterns. Flood modelers thus often face the problem that the true surface water extent is unknown and cannot be systematically mapped at the appropriate scale and spatial resolution. This paper presents a UAS thermal mapping workflow that can deliver surface water extent maps at a native spatial resolution better than 10cm, depending on the flight height. Based on comparisons with the Bluespot product derived from the national elevation model of Denmark and on informal flood observations in the study areas (i.e. ground-based photography at flooded locations), we are confident that the UAS mapping workflow delivers SWE maps that are close to the actual inundation patterns on the ground, for areas without dense vegetation cover.

Despite the high fidelity of flood maps delivered by the UAS mapping workflow, the workflow is not suitable for operational flood monitoring and surveillance at high temporal resolution and wide spatial coverage. Using multirotor platforms, UAS mapping workflows can cover areas of about a few square kilometers per day. Spatial coverage can be significantly increased using fixed-wing platforms, but regional-scale operational monitoring remains impractical. Thus, satellite EO and/or models will remain the methods of choice for operational flood monitoring at regional scale. However, models and workflows based on satellite EO need to be validated and benchmarked against high-fidelity datasets in order to assess and document their skillfulness. UAS flood maps can play a key role in this context, because they provide reliable inundation maps at very high spatial resolution. Our study shows that a flood mapping workflow based on public data from the Sentinel missions reliably maps permanent water bodies in the chosen test regions, while small-scale flooding caused by excess rainfall on grasslands and agricultural fields is not identified with confidence. Sentinel-2 flood maps show a higher number of true positives when compared to UAS flood maps than Sentinel-1 flood maps. However, unlike Sentinel-1 SAR, Sentinel-2 spectral mapping is not possible under cloud cover, which severely restricts the temporal resolution of flood maps. Overall, it seems that UAS mapping reliably detects flooding in the right places, while the spatial resolution of Sentinel datasets seems to be insufficient to detect small-scale flooding. Higher spatial resolution commercial alternatives to the Sentinel missions exist (e.g. TerraSAR-X, [25]) but come at a higher cost. Depending on the intended application of the mapping workflow, appropriate data value analysis should therefore be carried out to ensure that additional costs are justified in terms of the enhanced skill of predictions. Such evaluations must be based

 doi:10.20944/preprints202210.0449.v1

on the comparison of predicted flood maps with "ground truth" for selected events in the historical record. UAS mapping workflows can play a key role in this context as they can provide high-fidelity, high-resolution flood maps for selected areas and events.

5. Conclusions

We conclude that UAS thermal mapping is an efficient surveying technique that delivers SWE maps with high fidelity and high spatial resolution for intermediate scales ranging up to a few square kilometers. Such high fidelity flooding maps are useful to calibrate, benchmark and validate models and flood mapping algorithms based on satellite earth observation.

Author Contributions: Peter Bauer-Gottwein conceived the study, performed the analysis of the data and drafted the manuscript. Henrik Grosen performed the thermal UAS surveys, low-level processing of the thermal maps and revised the draft manuscript. Daniel Druce performed the satellite EO data processing and revised the draft manuscript. Christian Tøttrup, Roland Löwe and Heidi E. Johansen validated the results and revised the draft manuscript.

Funding: This study was supported by Innovation Fund Denmark through the ChinaWaterSense project (File number: 8087-00002B)

Data Availability Statement: Satellite EO and UAS flooding maps are available as geotiff raster maps in the supplementary material of this article. The national elevation dataset and Bluespot product can be downloaded from [20,21,24].

Conflicts of Interest: The authors declare no conflict of interest.

References

1. Wang, Y.; Chen, A.S.; Fu, G.; Djordjević, S.; Zhang, C.; Savić, D.A. An Integrated Framework for High-Resolution Urban Flood Modelling Considering Multiple Information Sources and Urban Features. *Environ. Model. Softw.* **2018**, *107*, 85–95, doi:10.1016/j.envsoft.2018.06.010.
2. Alfieri, L.; Pappenberger, F.; Wetterhall, F.; Haiden, T.; Richardson, D.; Salamon, P. Evaluation of Ensemble Streamflow Predictions in Europe. *J. Hydrol.* **2014**, *517*, 913–922, doi:10.1016/j.jhydrol.2014.06.035.
3. Alfieri, L.; Burek, P.; Dutra, E.; Krzeminski, B.; Muraro, D.; Thielen, J.; Pappenberger, F. GloFAS-Global Ensemble Streamflow Forecasting and Flood Early Warning. *Hydrol. Earth Syst. Sci.* **2013**, *17*, 1161–1175, doi:10.5194/hess-17-1161-2013.
4. Winsemius, H.C.; Van Beek, L.P.H.; Jongman, B.; Ward, P.J.; Bouwman, A. A Framework for Global River Flood Risk Assessments. *Hydrol. Earth Syst. Sci.* **2013**, *17*, 1871–1892, doi:10.5194/hess-17-1871-2013.
5. Neal, J.; Schumann, G.; Bates, P. A Subgrid Channel Model for Simulating River Hydraulics and Floodplain Inundation over Large and Data Sparse Areas. *Water Resour. Res.* **2012**, *48*, doi:https://doi.org/10.1029/2012WR012514.
6. Hall, J.W.; Tarantola, S.; Bates, P.D.; Horritt, M.S. Distributed Sensitivity Analysis of Flood Inundation Model Calibration. *J. Hydraul. Eng.* **2005**, *131*, 117–126, doi:10.1061/(ASCE)0733-9429(2005)131:2(117).
7. Yamazaki, D.; Ikeshima, D.; Sosa, J.; Bates, P.D.; Allen, G.H.; Pavelsky, T.M. MERIT Hydro: A High-Resolution Global Hydrography Map Based on Latest Topography Dataset. *Water Resour. Res.* **2019**, *55*, 5053–5073, doi:10.1029/2019WR024873.
8. Guth, P.L.; Geoffroy, T.M. LiDAR Point Cloud and ICESat-2 Evaluation of 1 Second Global Digital Elevation Models: Copernicus Wins. *Trans. GIS* **2021**, *25*, 2245–2261, doi:10.1111/tgis.12825.
9. Schneider, R.; Tarpanelli, A.; Nielsen, K.; Madsen, H.; Bauer-Gottwein, P. Evaluation of Multi-Mode CryoSat-2 Altimetry Data over the Po River against in Situ Data and a Hydrodynamic Model. *Adv. Water Resour.* **2018**, *112*, 17–26, doi:10.1016/j.advwatres.2017.11.027.
10. Pekel, J.-F.; Cottam, A.; Gorelick, N.; Belward, A.S. High-Resolution Mapping of Global Surface Water and Its Long-Term Changes. *Nature* **2016**, *540*, 418–422, doi:10.1038/nature20584.
11. Donchyts, G.; Baart, F.; Winsemius, H.; Gorelick, N.; Kwadijk, J.; van de Giesen, N. Earth's Surface Water Change over the Past 30 Years. *Nat. Clim. Chang.* **2016**, *6*, 810–813, doi:10.1038/nclimate3111.
12. Salamon, P.; Mctlormick, N.; Reimer, C.; Clarke, T.; Bauer-Marschallinger, B.; Wagner, W.; Martinis, S.; Chow, C.; Böhnke, C.; Matgen, P.; et al. The New, Systematic Global Flood Monitoring Product of the Copernicus Emergency Management Service. In Proceedings of the 2021 IEEE International Geoscience and Remote Sensing Symposium IGARSS; 2021; pp. 1053–1056.
13. Manfreda, S.; McCabe, M.F.; Miller, P.E.; Lucas, R.; Madrigal, V.P.; Mallinis, G.; Dor, E.B.; Helman, D.; Estes, L.; Ciraolo, G.; et al. On the Use of Unmanned Aerial Systems for Environmental Monitoring. *Remote Sens.* **2018**, *10*, doi:10.3390/rs10040641.
14. Herbst, V.; Grage, T. *Euroheat and Power/Fernwarme International*. 2020, pp. 34–39.
15. Berni, J.A.J.; Zarco-Tejada, P.J.; Suárez, L.; Fereres, E. Thermal and Narrowband Multispectral Remote Sensing for Vegetation Monitoring from an Unmanned Aerial Vehicle. *IEEE Trans. Geosci. Remote Sens.* **2009**, *47*, 722–738, doi:10.1109/TGRS.2008.2010457.
16. Ezenne, G.I.; Jupp, L.; Mantel, S.K.; Tanner, J.L. Current and Potential Capabilities of UAS for Crop Water Productivity in Precision Agriculture. *Agric. Water Manag.* **2019**, *218*, 158–164, doi:10.1016/j.agwat.2019.03.034.
17. Tauro, F.; Grimaldi, S. Ice Dices for Monitoring Stream Surface Velocity. *J. Hydro-Environment Res.* **2017**, *14*, 143–149, doi:10.1016/j.jher.2016.09.001.
18. Drone Systems. Thermal Orthomaps Available online: https://dronesystems.dk/en/our-activities/thermal-orthomaps/ (accessed on 20 September 2022).
19. Styrelsen for Dataforsyning og Infrastruktur. The Danish Elevation Model (DK-DEM) Available online:

https://eng.sdfi.dk/products-and-services/the-danish-elevation-model-dk-dem (accessed on 20 September 2022).

20. Styrelsen for Dataforsyning og Infrastruktur. Danmarks Højdemodel - Overflade Available online: https://dataforsyningen.dk/data/928 (accessed on 20 September 2022).
21. Styrelsen for Dataforsyning og Infrastruktur. Danmarks Højdemodel - Terræn Available online: https://dataforsyningen.dk/data/930 (accessed on 20 September 2022).
22. Druce, D.; Tong, X.; Lei, X.; Guo, T.; Kittel, C.M.M.; Grogan, K.; Tottrup, C. An Optical and SAR Based Fusion Approach for Mapping Surface Water Dynamics over Mainland China. *Remote Sens.* **2021**, *13*, doi:10.3390/rs13091663.
23. Tottrup, C.; Druce, D.; Meyer, R.P.; Christensen, M.; Riffler, M.; Dulleck, B.; Rastner, P.; Jupova, K.; Sokoup, T.; Haag, A.; et al. Surface Water Dynamics from Space: A Round Robin Intercomparison of Using Optical and SAR High-Resolution Satellite Observations for Regional Surface Water Detection. *Remote Sens.* **2022**, *14*, doi:10.3390/rs14102410.
24. Styrelsen for Dataforsyning og Infrastruktur. Danmarks Højdemodel - Bluespot Available online: https://dataforsyningen.dk/data/2698 (accessed on 20 September 2022).
25. Krieger, G.; Moreira, A.; Fiedler, H.; Hajnsek, I.; Werner, M.; Younis, M.; Zink, M. TanDEM-X: A Satellite Formation for High-Resolution SAR Interferometry. *IEEE Trans. Geosci. Remote Sens.* **2007**, *45*, 3317–3340, doi:10.1109/TGRS.2007.900693.